catalysts

Article

Visible Light-Driven Organic Pollutant Removal Using Fe-Based Photocatalysts Supported by Wheat Straw Biochar

Mahesan Naidu Subramaniam [1], Jiaojiao Zheng [1], Zhentao Wu [1,*], Pei Sean Goh [2] and Guangru Zhang [3]

[1] Energy and Bioproducts Research Institute, Aston University, Aston St, Birmingham B4 7ET, UK; m.subramaniam1@aston.ac.uk (M.N.S.); jzhen20@aston.ac.uk (J.Z.)
[2] Advanced Membrane Technology Research Center, University Teknologi Malaysia, Skudai 81300, Johor, Malaysia; peisean@petroleum.utm.my
[3] State Key Laboratory of Materials-Oriented Chemical Engineering, College of Chemical Engineering, Nanjing Tech University, 30 Puzhu Road(S), Nanjing 211816, China; guangru.zhang@njtech.edu.cn
* Correspondence: z.wu7@aston.ac.uk

Abstract: Researchers are actively pursuing the development of highly functional photocatalyst materials using environmentally friendly and sustainable resources. In this study, wheat straw biochar (BC), a by-product of biomass pyrolysis, was explored as a green, porous substrate and a carbon-based sensitizer to activate Fe-based photocatalysts under visible light. The research also delved into the impact of doping copper (Cu), chromium (Cr), and zinc (Zn) to enhance the photocatalytic activity of BC-Fe-based catalysts for the removal of methylene orange (MO) from water. Characterization results revealed a more than twofold increase in surface area and greater porosity, contributing to improved radical generation. BC demonstrated its dual functionality as a high surface area substrate and an electron sink, facilitating multistep electron movement and enhancing the photoactivity of the composite catalyst. Photodegradation experiments indicated that the combination of BC with Fe and Zn exhibited the highest performance, removing over 80% of MO within 120 min. Parametric studies highlighted the preference for an alkali pH, and the photocatalyst demonstrated efficient performance up to 30 ppm of dye. Radical scavenging experiments identified •OH and h^+ as the most generated radicals. This study establishes that the green and sustainable BC holds promise as a material in the quest for more sustainable photocatalysts.

Keywords: biochar; visible light photocatalysis; Fe-based photocatalyst; metal doping; methylene orange

check for updates

Citation: Subramaniam, M.N.; Zheng, J.; Wu, Z.; Goh, P.S.; Zhang, G. Visible Light-Driven Organic Pollutant Removal Using Fe-Based Photocatalysts Supported by Wheat Straw Biochar. *Catalysts* **2024**, *14*, 43. https://doi.org/10.3390/catal14010043

Academic Editor: Maria Victoria Lopez-Ramon

Received: 1 December 2023
Revised: 19 December 2023
Accepted: 5 January 2024
Published: 8 January 2024

1. Introduction

Water scarcity and pollution have been a prominent global issue over time due to increased population, energy consumption, industrial pollution and climate change [1]. One of the main industries that consumes large quantities of water is the textile industry [2]. Synthetic dyes are increasingly being identified as a highly hazardous organic pollutants due to their inherent complex structures, stability in aqueous environments, and toxicity in water [3]. The nature of the manufacturing process in the textile industry leads to the generation of large volumes of wastewater, which can be detrimental if left untreated [4,5]. The presence of such dye molecules in water bodies can pose various threats to the environment and the organisms living in it, as it can absorb sunlight, increase chemical oxygen demand in water bodies, and inhibit the growth of aquatic species [6]. Current methods to treat such wastewater include physical treatments such as coagulation and flocculation, filtration and adsorption [7], while biological treatment methods such as aerobic and aeration ponding can be challenging due to the chemical stability (aromatic rings) of commercial dye molecules [8,9]. Photocatalysis has been considered as a viable approach to remove chemically stable compounds, due to its ability to generate radical oxidative species (ROS). Extensive research has focused on designing and refining metal based photocatalysts, with an emphasis in developing a greener catalyst with metal dopants to enhance its photocatalytic efficiency [10,11].

There have been various attempts to modify photocatalysts to improve their inherent properties. Among others is the employment of materials which can serve as a substrate and electron sink [12,13]. Biochar (BC) is a green carbon-based product derived from pyrolyzing biomass feedstocks [14]. With its abundance, stability, and porous nature, BC has been considered as an ideal substrate material of photocatalysts by providing many active sites for efficient catalytic reactions [15]. Moreover, carbon in the BC serves as a non-metallic dopant and enhances the photoactivity of metal photocatalysts [16,17]. Carbon does not possess semiconducting properties, which necessitates the use of a semiconducting material to serve as the photocatalyst. While various carbon-based dopants such as graphene [18,19], carbon dots (CDs) [20,21], carbon nanotubes [22], and reduced graphene oxide [23,24] have been intensely explored, the use of BC as a carbon-based dopant source for photocatalysts has been scarcely reported. Eltaweil et al. used BC as a nanocomposite to grow silver (Ag) photocatalysts for the photodegradation of methylene blue (MB) dyes in water streams [25]. The graphitic structure of BC was able to ameliorate the interfacial charge separation, thus quenching the recombination electron–hole pairs, which in turn improve the generation of reactive oxygen species (ROS) that drive the photocatalytic degradation process. Furthermore, the porous nature of BC enables a higher number of photocatalysts to be deposited, increasing the number of active sites compared to conventional photocatalysts. It is imperative that the use of green resources available in the field of photocatalysis has been carried out at a rapid pace to enhance the sustainability of the technology [10,25]. Recent work on the development of BC derived from algae on titania nanotube arrays showed promising result in removing methylene blue (MB), where an improvement in charge carrier separation, inducing multistep charge transfer, and electron transfer have been identified as the main contributor to the improvement in photoactivity [26]. Moreover, the current body of literature lacks comprehensive coverage of bi-metallic photocatalysts using BC as both a substrate and as an electron sink. While the use of bimetallic photocatalysts has shown clear advantages over traditional photocatalysts, including i) enabling temporary intermediates, ii) modifying activation energy upon adsorption, and iii) varied electron transfer, the incorporation of BC in the synthesis of bi-metallic photocatalysts has further potential. They include synergistically reducing recombination rates, narrowing of the band gap, and an enhancement of contact between pollutants and the photocatalyst. To address this gap in the literature, we would employ metals such as Cu, Cr, and Zn as the co-dopants for Fe-based photocatalysts.

In this study, a BC-based Fe photocatalyst was synthesized using a facile chemical precipitation method. BC was produced from locally sourced wheat straw in the United Kingdom, serving as a feasible biomass for creating a porous BC substrate. In this context, Fe was assigned the role of the active photocatalyst, while BC functions as an eco-friendly, porous substrate to accommodate the photocatalyst. Fe is a good semiconducting material and is an established choice of photocatalyst in the literature, while BC is not a semiconducting material. On the other hand, BC also acts as an electron sink during the photoactivation process. To develop the bimetallic photocatalysts, the Fe-based photocatalyst was doped with Cu, Cr, or Zn to investigate the interactions between metallic dopants and elucidate the potential synergies of enhancing the photocatalytic activity of the prepared catalysts. The synthesized photocatalysts underwent thorough characterizations, including scanning electron microscopy, transmission electron microscopy, energy-dispersive X-ray spectroscopy, X-ray diffraction, porosimetry, zeta potential measurement, fluorescence spectroscopy, and ultraviolet-visible-near infrared absorption for visible light. The efficacy of the prepared catalyst was then assessed in terms of its photocatalytic performance under visible light conditions, utilizing methylene orange (MO) as the model pollutant. Various parameters such as the initial concentration of MO and the pH of MO were systematically studied. Moreover, an examination of the photocatalyst's recyclability and stability was conducted to enhance the comprehensive understanding of its practical applicability. The future of bio-based photocatalysts in wastewater treatment appears promising, providing efficient pollutant elimination for water purification. Their sustainability and cost-effectiveness are essential attributes in the development of environmentally friendly solutions to tackle global water scarcity and improve the overall robustness of wastewater treatment systems.

2. Results and Discussion

2.1. Characterization of Catalyst

Figure 1 shows the scanning electron microscopy images of BC, BC-Fe-Cu, BC-Fe-Cr and BC-Fe-Zn. The images reveal the well-defined inner wall structure of the BC substrates even at a pyrolysis temperature of 500 °C. As shown in Figure 1a, BC exhibits a clear surface without any fragments after pyrolysis with little impurity or debris. Conversely, other samples (Figure 1b–d) exhibit particulate matters present on the BC surface. These particulates are the composite metals co-precipitated onto the BC surface. This is similar to the work of Wang et al. [27], where Ti-based photocatalysts were deposited onto the surface of the BC substrate. The transmission electron microscopy image as elucidated in Figure 1e shows the deposition of both Fe and Zn on the structure of BC. In addition to this, Figure 1f clearly shows the lattice structure of both the nanoparticles deposited on the surface of the BC, where the spacing between two adjacent lattice fringes of Fe nanoparticles is 2.59 ± 0.04 Å (104), whereas the spacing of the Zn nanoparticle is calculated as 4.66 ± 0.04 Å (102). These spacings correspond to the (104) planes of α-Fe_2O_3 and the (102) planes of ZnO [28,29].

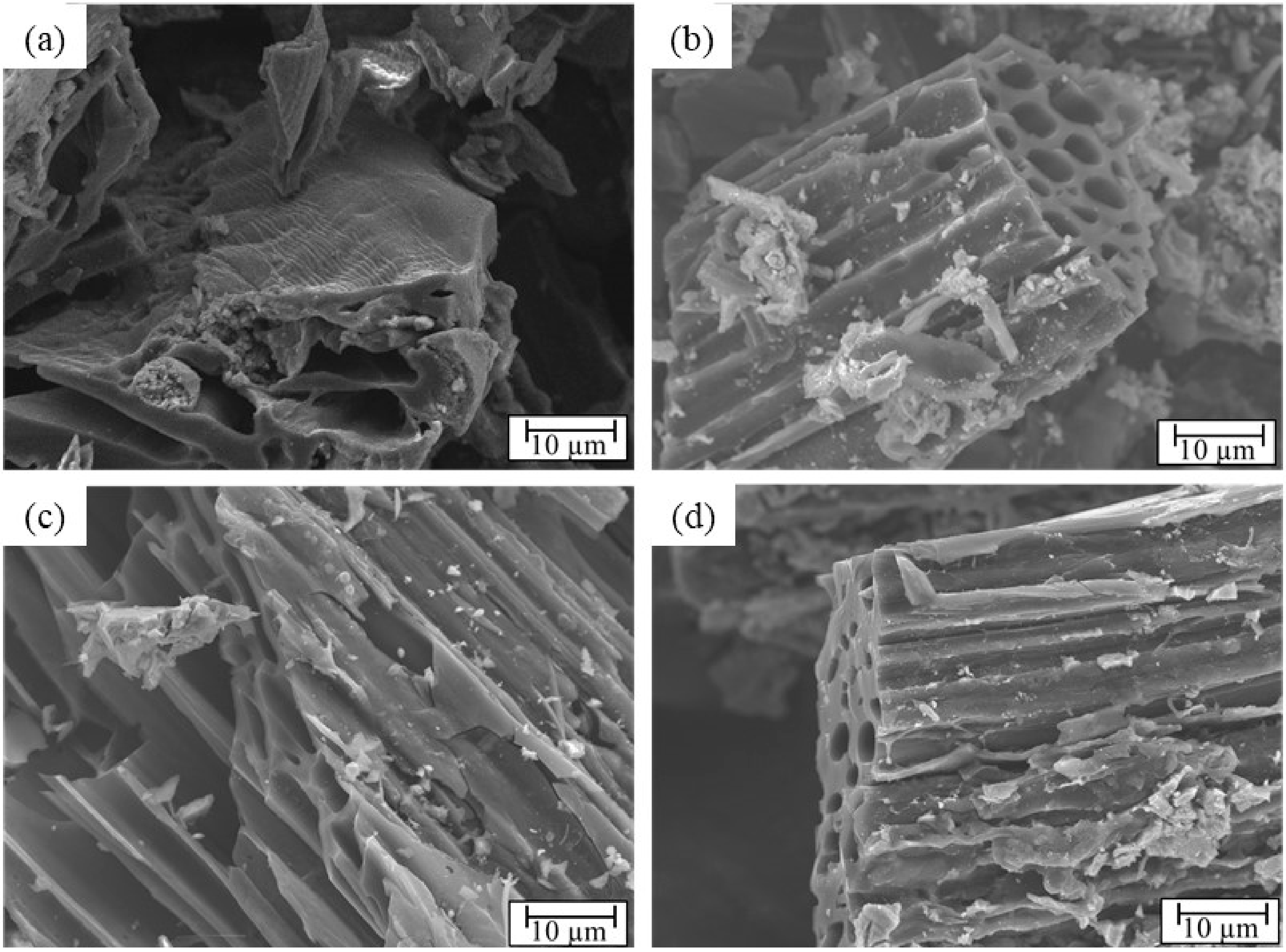

Figure 1. *Cont.*

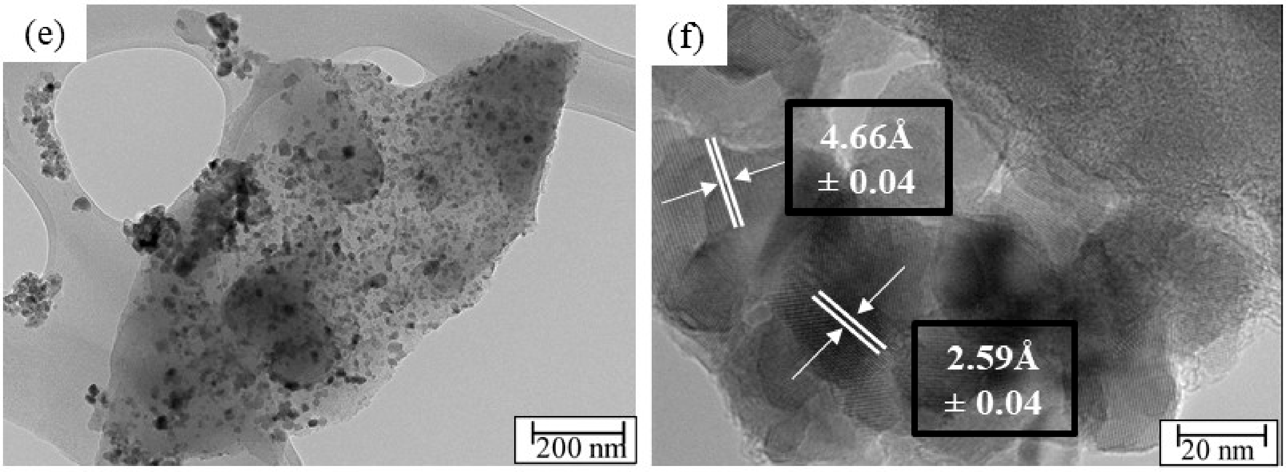

Figure 1. Scanning electron microscopy images of (**a**) BC, (**b**) BC-Fe-Cu, (**c**) BC-Fe-Cr and (**d**) BC-Fe-Zn at a magnification of 1.8 K, and transmission electron microscopy images of (**e**) BC-Fe-Zn magnified at 30 K and (**f**) the lattice structure of BC-Fe-Zn magnified at 500 K.

Energy-dispersive X-ray spectroscopy analysis was conducted to observe and understand the growth of nanomaterials on the surface of the BC substrate. Figure 2 presents the energy-dispersive X-ray spectroscopy mapping, while Figure 3 shows the energy-dispersive X-ray spectroscopy spectra of BC-Fe, BC-Fe-Cu, BC-Fe-Cr, and BC-Fe-Zn, respectively. The mapping shows evidence that the iron (Fe) nanoparticles and subsequent dopants (Cu, Cr, Zn) were uniformly dispersed throughout the structure of the BC. These images highlight the successful distribution of both Fe and dopant nanoparticles on the BC surface. The closely packed surface morphology of the prepared BC composite photocatalyst is significant, as it supports efficient charge carrier separation [30]. The proximity between the photocatalyst and BC, acting as a substrate and an electron sink, is advantageous for prolonging the photocatalytic activation of the composite photocatalyst. Energy-dispersive X-ray spectroscopy analyses were also conducted on the samples to understand the dispersion of the Fe catalyst as well as the dopants on BC, which are shown in Figure 2. The energy-dispersive X-ray spectroscopy spectra showed an even distribution of Fe on the surface of BC. This is similar for the secondary dopants (Cu, Cr, Zn), as the energy-dispersive X-ray spectroscopy spectra overlaps with Fe, showcasing the formation of binary metallic catalysts. Moreover, the spectral analysis presented in Figure 3 indicates a higher concentration of Fe nanoparticles compared to their respective dopants in BC-Fe-Cu and BC-Fe-Cr. On the other hand, for BC-Fe-Zn, the dopant has a higher weightage. The ratios of Fe to Cu, Cr, and Zn in each photocatalyst were determined to be 2:1.7, 2:1.63, and 2:2.9, respectively. The higher dopant ratio for Zn can be ascribed to its greater electronegativity relative to Fe. Considering that the co-precipitation method was utilized in the development of the photocatalyst, the precipitation of Zn was prioritized over Fe due to its higher electronegativity.

The X-ray diffraction patterns of the photocatalysts are elucidated in Figure 4 with the peaks and their corresponding planes collated in Table 1. The BC exhibited a diffraction amorphous broad band with a maximum intensity at $2\theta = 23^\circ$. The broad peak between 20° and 30° refers to the stacking structure of aromatic layers (002), and the broadening was originated from the small dimensions of crystallites perpendicular to aromatic layers, which was also identified in other studies [31,32]. This broad peak disappeared for all the BC–metal samples. The crystalline phase of all the other metals deposited on the surface of BC was also identified and collated in Table 1. All the photocatalysts incorporated with metal lack the amorphous region exhibited by BC at 2θ of 20° to 30°, indicating that the amorphous region changed into crystalline structures due to calcination at 500 °C as well as the incorporation of various metal particles. All the modified samples exhibited the characteristic peaks of Fe (311, 440), while characteristic peaks of Cu [33,34], Cr [35], and Zn [36] were also evident in the respective X-ray diffraction spectra. Small shifts in the Fe peaks in the X-ray diffraction spectra of the bimetallic photocatalyst, such as for (220), (440) and (311), are observed. The samples with such peak shifts can be due to the changes in the lattice parameters and defect density. The presence of the peaks (104) for planes of α-Fe_2O_3 and (102) for planes of ZnO in BC-Fe-Zn also corresponds to the lattice spacing calculation based on the transmission electron microscopy images shown in Figure 1. Scherrer's equation was employed to assess the crystalline size based on intense X-ray diffraction spectral peaks for each photocatalyst. The crystalline sizes for BC, BC-Fe, BC-Fe-Cu, BC-Fe-Cr, and BC-Fe-Zn are 1.86 ± 0.4 nm, 7.59 ± 0.5 nm, 5.72 ± 0.5 nm, 3.9 ± 0.4 nm, and 16.34 ± 1.9 nm, respectively. The larger crystalline size of BC-Fe-Zn may be attributed to the higher electronegativity of Zn compared to the other dopants, leading to the formation of larger crystal sizes. BC exhibits a small crystal size due to its more disordered amorphous regions compared to ordered crystalline regions before the growth of metal nanoparticles on them [37].

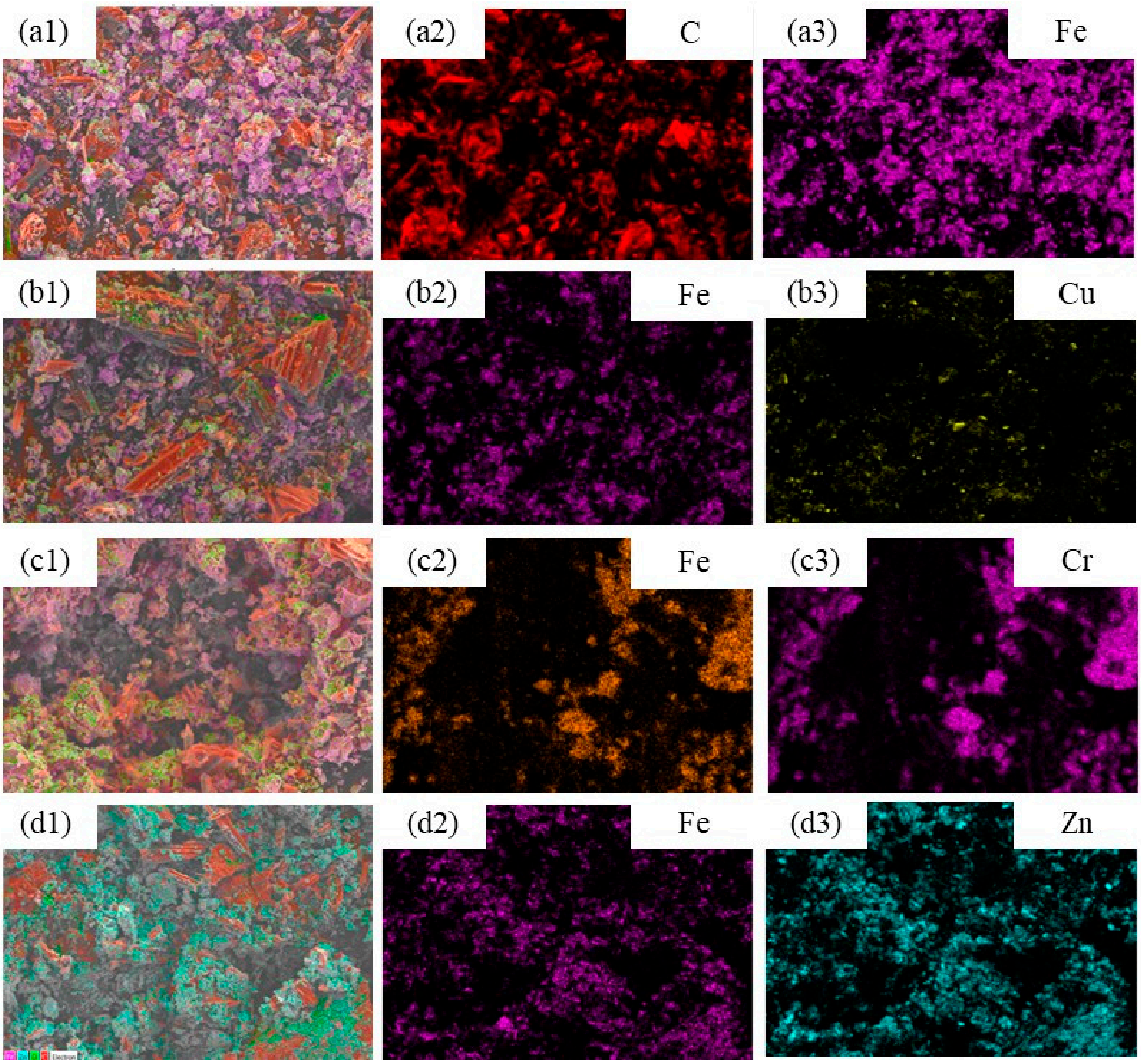

Figure 2. Energy-dispersive X-ray spectroscopy mapping of BC-Fe (**a1**–**a3**), BC-Fe-Cu (**b1**–**b3**), BC-Fe-Cr (**c1**–**c3**) and BC-Fe-Zn (**d1**–**d3**).

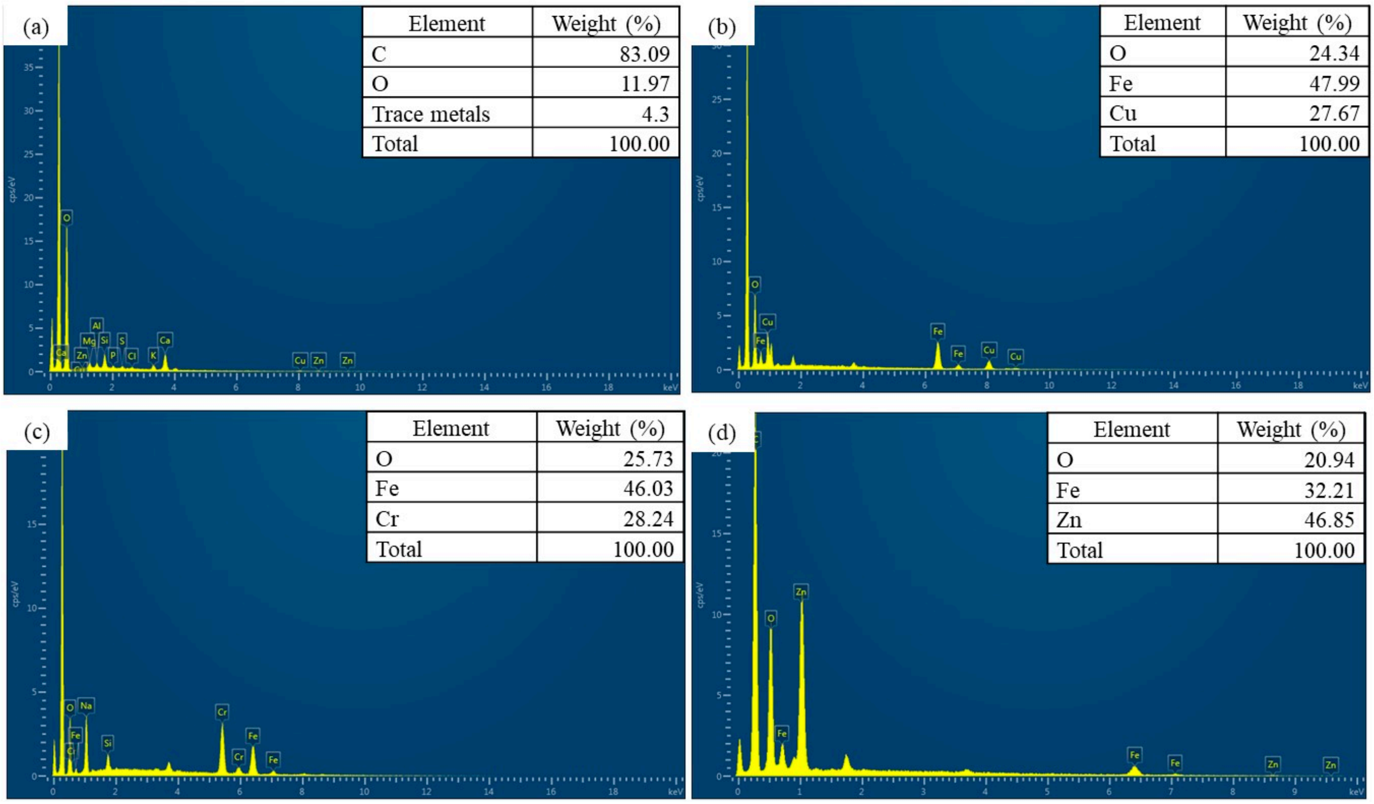

(a)

Element	Weight (%)
C	83.09
O	11.97
Trace metals	4.3
Total	100.00

(b)

Element	Weight (%)
O	24.34
Fe	47.99
Cu	27.67
Total	100.00

(c)

Element	Weight (%)
O	25.73
Fe	46.03
Cr	28.24
Total	100.00

(d)

Element	Weight (%)
O	20.94
Fe	32.21
Zn	46.85
Total	100.00

Figure 3. Energy-dispersive X-ray spectroscopy spectra for (**a**) pristine BC, (**b**) BC-Fe-Cu, (**c**) BC-Fe-Cr, and (**d**) BC-Fe-Zn (inset: elemental weight based on individual composite photocatalyst's EDS spectra analysis).

Table 1. X-ray diffraction planes of the photocatalysts prepared in this work.

Sample	2θ (Corresponding Planes)
BC	26.3° (200), 28.2° (002), 39.3° (220), 40.3° (100), 59.4° (400)
BC-Fe	26.6° (220), 35.7° (311), 59.9° (511), 62.9° (440)
BC-Fe-Cu	30.6° (110), 35.5° (311), 36.3° (110), 43.2° (111), 62.7° (440)
BC-Fe-Cr	27.4° (220), 35.7° (311), 63.1° (220), 62.6° (440)
BC-Fe-Zn	29.8° (100), 35.2° (311), 39.9° (110), 42.7° (113) 53.1° (110), 59.6° (102), 62.2° (200) (440)

Table 2 presents the compiled results, including the specific surface area (SSA), average pore volume, average pore diameter, and zeta potential for all the catalysts prepared in this study. It is noteworthy that there was a notable increase in the SSA of all the bimetallic photocatalysts compared to BC and the BC-Fe catalyst. The SSA, average pore volume and average pore diameter were determined using the BJH method, using N_2 as the adsorption gas of choice. The average BC-Fe-Cu and BC-Fe-Zn exhibited the highest SSA values at 119.41 m^2/g and 117.99 m^2/g, respectively, in contrast to BC's 41.07 m^2/g. BC-Fe-Cr also demonstrated a high SSA value of 102.27 m^2/g. Additionally, all the prepared catalysts exhibited an increase in pore volume with bimetallic photocatalysts showing values between 5.62 and 7.20 cm^3/g compared to BC's pore volume of 3.73 cm^3/g.

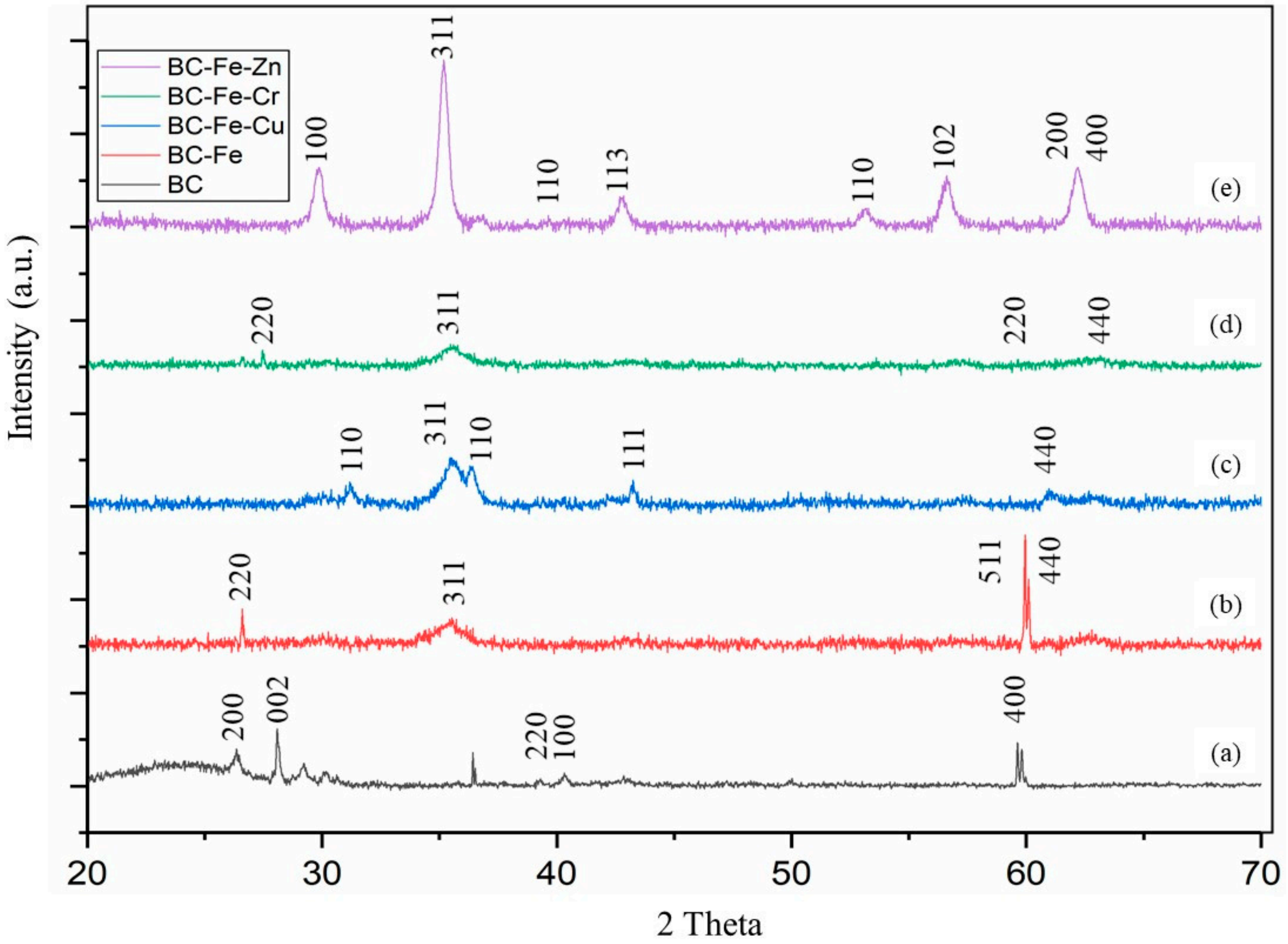

Figure 4. X-ray diffraction spectra of (**a**) BC, (**b**) BC-Fe, (**c**) BC-Fe-Cu, (**d**) BC-Fe-Cr and (**e**) BC-Fe-Zn.

Table 2. SSA, average pore volume, average pore diameter and zeta potential (pH 7) of the catalysts prepared in this work.

Material	SSA (m^2/g)	Average Pore Size (nm)	Average Pore Volume (cm^3/g)	Zeta Potential (mV)
BC	41.07 ± 1.1	3.09 ± 0.2	3.73 ± 0.5	−31.13
BC-Fe	55.26 ± 1.2	7.88 ± 0.5	10.42 ± 0.6	−21.23
BC-Fe-Cu	119.41 ± 0.9	2.01 ± 0.4	5.62 ± 0.6	−52.60
BC-Fe-Cr	102.27 ± 2.1	3.15 ± 0.3	7.37 ± 0.7	−30.87
BC-Fe-Zn	117.99 ± 1.8	2.72 ± 0.4	7.72 ± 0.8	−45.10

The use of a strong alkali agent during catalyst preparation (6M NaOH) played a role, as previous research has indicated that alkali agents can enhance the crystallinity of BC by dissolving the amorphous structure within it [36]. This is supported by the X-ray diffraction spectra of all NaOH-treated BC, as shown in Figure 4, which displayed the absence of an amorphous broad band with a maximum intensity at $2\theta = 23°$. Additionally, the use of alkali led to the removal of volatile components that may be blocking the BC substrate, as demonstrated in previous research [38]. The exfoliation of such porous substrates can also eliminate impurities, thereby increasing the material's porosity [5]. Regarding the pore size of the materials, no significant difference was observed between the BC samples and the bimetallic catalysts. However, the BC-Fe photocatalyst exhibited a significant increase in pore size compared to the others, which was similar to the trend observed for pore volume. This increase can be attributed to the exfoliation and removal of impurities from the raw BC by the strong NaOH used during co-precipitation [5]. Bimetallic photocatalysts may exhibit a smaller pore size and lower pore volume compared to the singular metallic photocatalyst (BC-Fe), as the concentration of precursor ions for bimetallic photocatalysts (0.6 M) was almost double that of the singular photocatalyst (0.4 M). This difference could lead to increased metal growth in the BC pores, resulting in a smaller pore size and lower pore volume, as indicated in Table 2 [39].

To comprehend the interaction between BC and the photocatalyst, the visible light response and band gap of the prepared photocatalyst were examined [40]. Additionally, the optical properties of the prepared catalyst were investigated through ultraviolet-visible spectroscopy analysis and fluorescence spectroscopy. Figure 5 presents the plot of the Kubelka–Munk function against photon energy and the fluorescence spectroscopy analysis for all the photocatalysts prepared in this study.

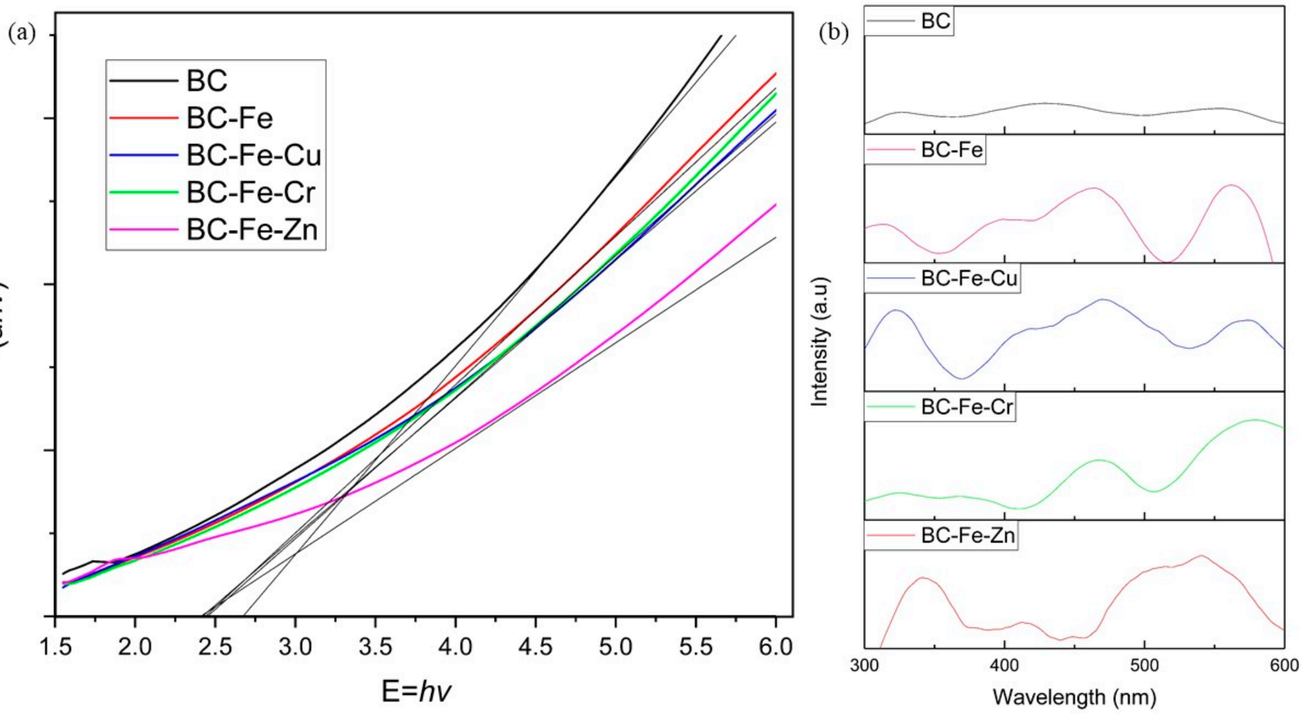

Figure 5. (**a**) Kubelka–Munk function, band gap calculation and (**b**) normalized fluorescence spectroscopy spectra of BC, BC-Fe, BC-Fe-Cu, BC-Fe-Cr and BC-Fe-Zn.

Studies in the literature have shown that the reduction in band gap can lead to improved photocatalytic activity. Additionally, a band gap of less than 3.2 eV would confirm that the photocatalyst is responsive toward visible light activation [41]. The band gap calculated based on the Kubelka–Munk function is 2.715, 2.423, 2.421, 2.424, and 2.403 eV for BC, BC-Fe, BC-Fe-Cu, BC-Fe-Cr and BC-Fe-Zn, respectively. Although BC by itself does not exhibit photoactivity, BC-based photocatalysts prepared in this work exhibited band gap values below 3.2 eV, indicating their visible light-induced photoactivity [42]. The band gap values were similar to those reported by Talukdar et al., where BC from bamboo exhibited a band gap value of 2.69 eV [43]. There is a very minimal difference in the band gap values with different dopants, i.e., Cu, Cr and Zn, as all three exhibited very similar band gap reductions when incorporated with BC-Fe [11]. The low molarity of the dopant can be considered as a factor for this, as the low amount is enough for band gap reduction. Photoluminescence analysis showed that BC exhibited neither light absorption nor emission. However, all the samples exhibited peaks at higher wave numbers in the visible range at different ranges, suggesting that they are responsive toward visible light. BC-Fe-Zn exhibited two large emission peaks at 350 and 550 nm, while BC-Fe, BC-Fe-Cu, and BC-Fe-Cr have similar peaks at 470 and 580 nm (BC-Fe-Cu has an additional emission peak at 320 nm) [44]. The photoluminescence spectra, together with the ultraviolet-visible spectroscopy results, can conclude that the photocatalysts prepared in this work are responsive toward visible light.

2.2. Adsorption Studies

In the photocatalytic process employing a heterogeneous catalyst, both adsorption and redox reactions occur simultaneously in the removal of the chosen pollutant. Therefore, it is crucial to comprehend the role played by the adsorption removal mechanism for different catalysts, enabling a more accurate interpretation of photocatalytic removal data. Figure 6 shows the adsorption trends of all the photocatalysts prepared in this work using MO (10 ppm).

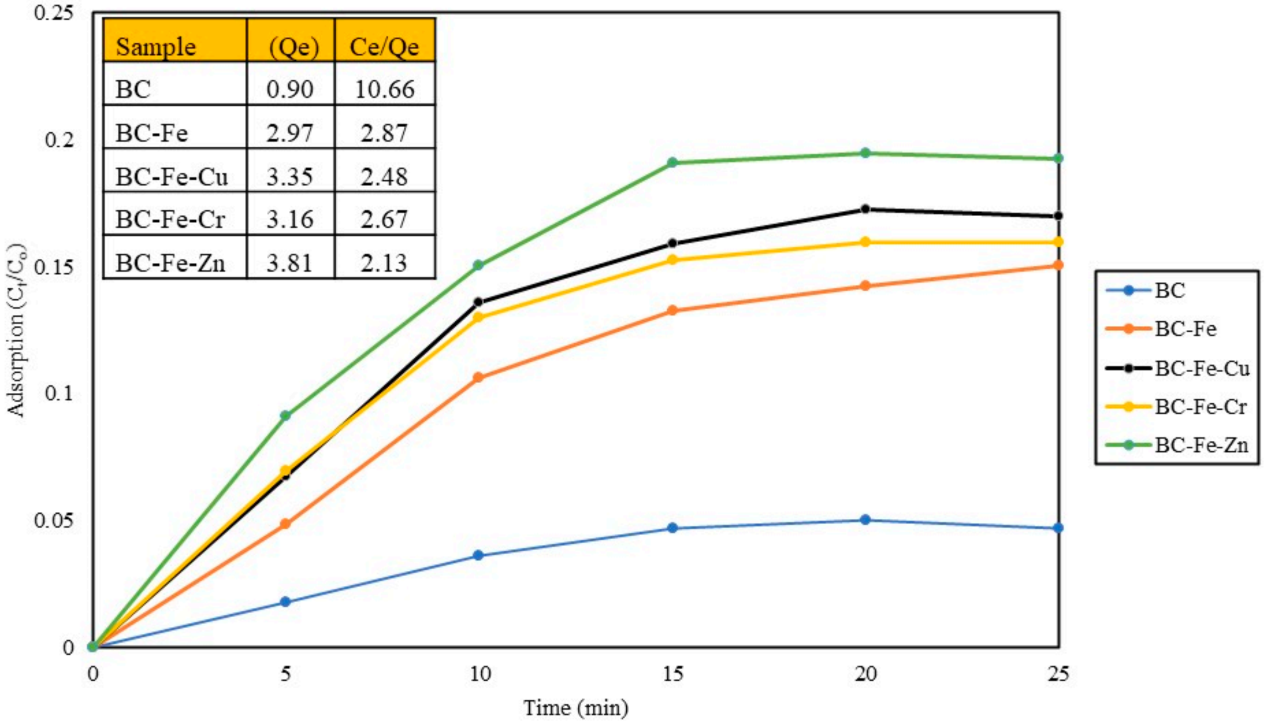

Sample	(Qe)	Ce/Qe
BC	0.90	10.66
BC-Fe	2.97	2.87
BC-Fe-Cu	3.35	2.48
BC-Fe-Cr	3.16	2.67
BC-Fe-Zn	3.81	2.13

Figure 6. Adsorption equilibrium pattern and adsorption capacity (inset) (Qe: adsorption equilibrium, Ce/Qe: adsorption capacity (mg/g)) of BC, BC-Fe, BC-Fe-Cu, BC-Fe-Cr and BC-Fe-Zn under dark conditions (catalyst loading = 1 g/L, pH = 7, MO concentration = 10 ppm, reaction time = 120 min, temperature = 25 °C, stirring = 250 rpm).

Adsorption studies were conducted to explore the adsorption equilibrium and capacity of the prepared photocatalyst. Adsorption capacity refers to the total amount in milligrams of a pollutant adsorbed per gram of adsorbate. In this study, all the modified photocatalysts exhibited a higher adsorption capacity for MO compared to pristine BC with a fourfold increase from 0.90 up to 3.81 mg/g for BC-Fe-Zn. The use of an alkali agent during the co-precipitation process facilitated the removal of impurities that blocked the extensive pore network of BC, resulting in an improved adsorption capacity. Additionally, the incorporation of metal dopants on the surface further enhanced the adsorption capacity, as evidenced by the increase in SSA. Moreover, based on Figure 6, it can be confirmed that the adsorption equilibrium is achieved approximately within 20 min.

2.3. Photocatalytic Activity of Prepared Catalyst

The photocatalytic activity of all the catalysts prepared in this work was evaluated based on their ability to effectively remove a model pollutant, MO. The effect of pH and initial concentrations of model pollutant as well as the recyclability of the photocatalysts were investigated in this study.

2.3.1. Effect of Different Metal Dopants on Photoactivity

Figure 7 shows the photocatalytic removal performance of all the photocatalyst prepared in this work under visible light conditions within 120 min. Table 3 shows the reaction constant and the regression line for pseudo-second-order kinetic reactions for all samples tested in this work. The experiment was started under dark conditions to allow adsorption equilibrium to be achieved. The preliminary studies implied that the reaction could be completed within 20 min.

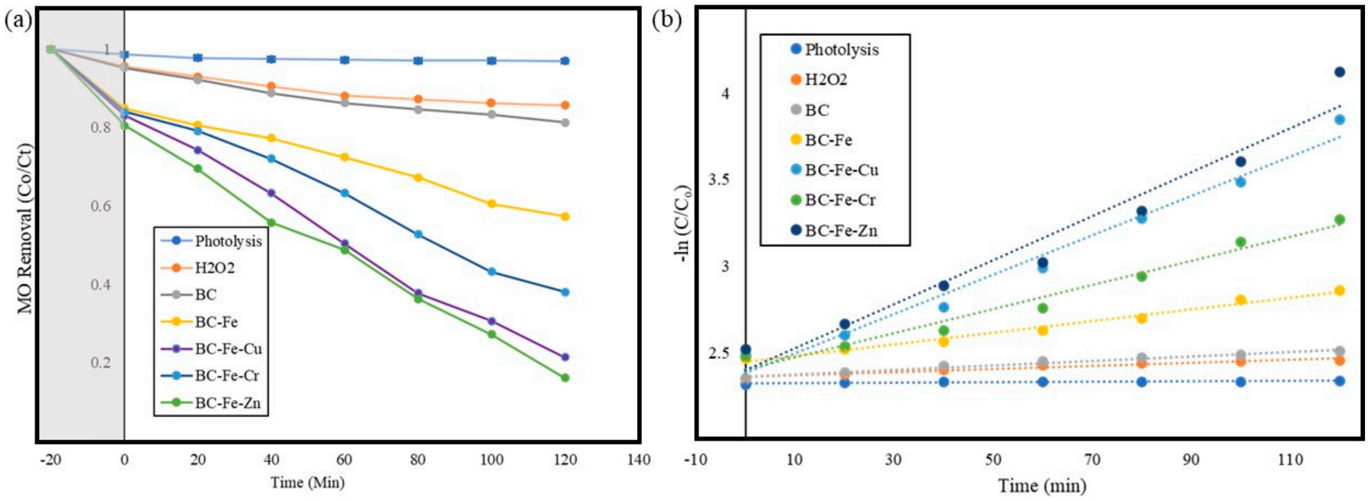

Figure 7. (**a**) Photocatalytic removal performance and (**b**) reaction kinetics of photolysis, BC, BC-Fe, BC-Fe-Cu, BC-Fe-Cr and BC-Fe-Zn under visible light conditions (catalyst loading = 1 g/L, pH = 7, MO concentration = 10 ppm, reaction time = 120 min, temperature = 25 °C, stirring = 250 rpm).

Table 3. Pseudo-first-order kinetics calculations: reaction rate constant and regression coefficients.

Samples	k (ppm min^{-1})	R^2
Photolysis	0.0181	0.8024
H_2O_2	0.0565	0.9413
BC	0.0585	0.9788
BC-Fe	0.5505	0.9833
BC-Fe-Cu	1.4477	0.9732
BC-Fe-Cr	0.9419	0.9768
BC-Fe-Zn	1.621	0.9531

It is a known fact that adsorption and photocatalytic removal happen in tandem. In this case, adsorption contributed to almost 20% of MO removal, where BC-Fe-Zn experienced MO adsorption of 19%, which was followed by BC-Fe-Cr at 16% and BC-Fe-Cu at 17%. There is some form of MO removal when BC was used, which is probably due to adsorption. BC-Fe-Zn shows the most promising result in regard to the combined adsorption and photocatalytic removal of MO, where 83.8% of MO was removed within the reaction time of 120 min. Among the dopants used, Zn has the smallest calculated atomic radii, with 142 pm, compared to Cu (145 pm) and Cr (166 pm). Wang et al. suggested in their work on the development of a FeCu@BC photocatalyst that the smaller atomic radius of the dopant indicates quicker ion migration and diffusion on the surface of the photocatalyst. This can lead to an enhancement of ion diffusions, which in turn could significantly improve the charge transfer ability and facilitate faster ion movement [45]. The improved charge transfer process can also promote the generation of active radical species. These can explain the superior performance of the photocatalytic exhibited by BC-Fe-Zn among others. Furthermore, evidence in the literature has also shown that photocatalysts with a larger crystalline size, as shown in the larger crystalline size of BC-Fe-Zn (16.34 ± 1.9 nm) compared to the other photocatalyst (BC-Fe: 7.59 ± 0.5 nm, BC-Fe-Cu: 5.72 ± 0.5 nm, BC-Fe-Cr: 3.9 ± 0.4 nm), exhibit superior photocatalytic performance [46]. The photoactivity via photolysis and the addition of H_2O_2 were also evaluated. The results show that photolysis has negligible ability to remove MO, while the addition of H_2O_2 was able to initiate some form of photocatalytic removal. Herein, up to 15% of MO was removed within the reaction time of 120 min. BC exhibited some form of adsorption and photoactivity, as it was able to remove up to 18.7% of MO, where 4.8% of the MO was initially removed via adsorption. All the other photocatalysts prepared in this work were able to exhibit adequate photoactivity, where BC-Fe, BC-Fe-Cu and BC-Fe-Cr were able to remove up to 42.7%, 78.7% and 62.0%, respectively. The regression lines for all the bimetallic catalysts tested showed a value of R2 > 0.95, which indicates that the data fit well with pseudo-second-order reaction kinetics model. It has to be noted that all bimetallic photocatalysts exhibited higher photocatalytic removal efficiency compared to the undoped BC-Fe photocatalyst prepared in this work.

2.3.2. Effect of Different pH Values and Different Initial Concentration

The impact of various pH values of MO used during the photocatalytic reaction was assessed for all the catalysts prepared in this study. Figure 8 illustrates the variations in MO removal efficiency under different pH conditions using all the photocatalysts prepared in this work.

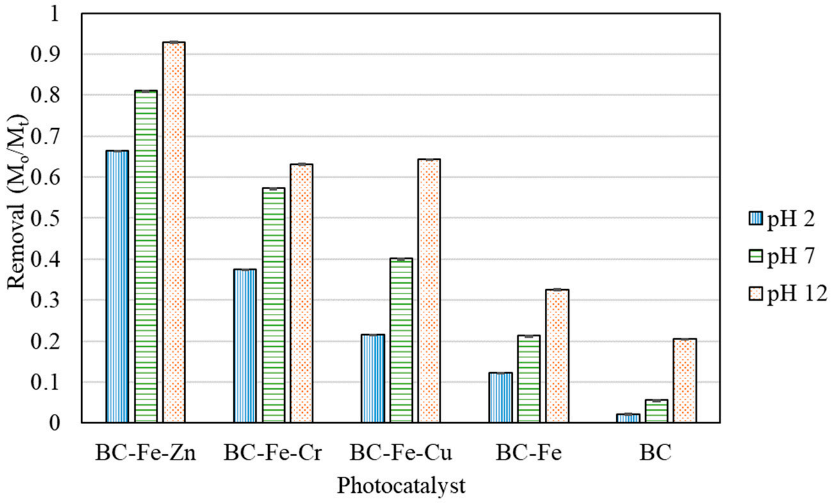

Figure 8. Removal of MO by all the photocatalysts prepared in this work at different pH values (catalyst loading = 1 g/L, pH = 2, 7 and 12, MO concentration = 10 ppm, reaction time = 120 min, temperature = 25 °C, stirring = 250 rpm).

Differing pH values of pollutants can significantly alter the physiochemical properties of pollutants in aqueous conditions. MO, which is used as the model pollutant in this work, is a common azo ionic dye used in the textile industry. MO possesses weak acidic properties, with a pH range between 3.1 and 4.4. In this work, the prepared MO exhibited a pH value of 3.9 ± 0.067. Modifying the pH value of the MO solution changed the surface characteristic, which greatly influenced both adsorption and photocatalytic removal efficiency. The results elucidated in Figure 8 show that all the catalysts experience enhanced photoactivity when the pH of the model pollutant is in the acidic range, whereas there is an inhibition in photoactivity when the pH is in the alkali range. This is consistent with the literature, as a similar phenomenon was also experienced in the research paper published by Modrogan et al. [47]. MO is anionic in nature due to the presence of its NH functional group. In acidic conditions, the surface of the catalyst prepared can acquire a negative charge, which would reduce its affinity toward the negatively charged MO molecules [48]. However, alkali conditions can increase the quantity of hydroxyl ions, which can be used to generate hydroxyl radicals under irradiation. Hence, the photocatalytic removal of MO is quicker under alkali conditions [49,50].

The increase in photoactivity can mainly be due to the improved interaction between the photocatalyst and MO molecules. The effect of the initial concentration of MO on the removal efficiency of BC-Fe-Zn was studied using concentrations of 10, 20, 30, 40 and 50 ppm. Figure 9 shows the photocatalytic removal efficiency of BC-Fe-Zn for MO as a function of initial concentration.

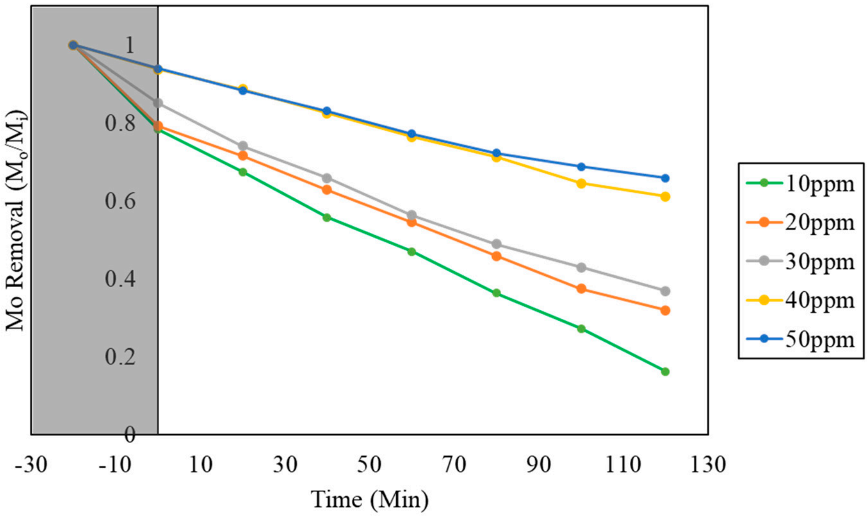

Figure 9. Photocatalytic removal of MO under different initial concentrations (10, 20, 30, 40, 50 ppm) (catalyst loading = 1 g/L, pH = 7, MO concentration = 10 ppm, reaction time = 120 min, temperature = 25 °C, stirring = 250 rpm).

It was observed that the change in initial concentration hindered the photocatalytic removal efficacy, especially at 40 and 50 ppm. There is a minimal difference in the effectivity between 10, 20 and 30 ppm, while there is a marked difference in efficiency when the initial concentration was increased to 40 ppm. The reduction in photocatalytic removal efficiency can be attributed to the increase in the number of dye molecules to be removed at a constant amount of catalyst present in the system [51]. The dye molecules were saturated in the solution, where the photocatalyst is not able to produce sufficient oxidative species to initiate a redox reaction within a short, designated timeframe. In addition to this, photocatalytic processes are surface-related phenomena, similar to adsorption [52]. Since adsorption happens before photocatalytic initiation, the saturation of MO on the surface of the catalyst can lead to a reduction in active sites available for photocatalytic activation. Similar experiments carried out for the photocatalytic removal of MO under different initial concentrations also showed that the range between 30 and 40 ppm was the threshold for a significant reduction in photocatalytic efficiency [53]. Here, it is imperative to note that the typical textile effluent can exhibit a concentration of dye within the range of 40–250 ppm. In such cases, a larger photocatalyst dosing would be required to manage such effluents. Hence, developing a photocatalyst with sustainable materials such as BC is imperative when considering large-scale applications which would require much larger dosages.

2.4. Recyclability of Photocatalyst and Radical Scavenging

Based on the previous experimental results, BC-Fe-Zn has been identified as the best-performing catalyst. The photocatalyst was further assessed in term of its recyclability.

The photostability, recyclability and reusability of the prepared photocatalyst is a crucial consideration for its practical application. To evaluate this, the photocatalyst's reusability was examined through five cycling tests aimed at removing MO under identical conditions. The results presented in Figure 10 show that BC-Fe-Zn exhibited only a slight reduction in its photoactivity over the course of five runs in the photocatalytic experiment. The minimal loss in photocatalyst performance may be due to the loss of photocatalyst particles during each round of collection and washing. Furthermore, the nature of MO which is soluble in dye also suggests that the adsorbed MO dye on the photocatalyst is not permanent; hence, it was able to be easily removed during the washing step. The adsorption of pollutant molecules on the surface of the photocatalyst is one common reason behind the loss of photoactivity, which was not observed in the work carried out [54]. These findings highlight the robustness and the stability of the prepared BC-Fe-Zn photocatalyst, demonstrating its ability to maintain exceptional MO removal even after five cycles.

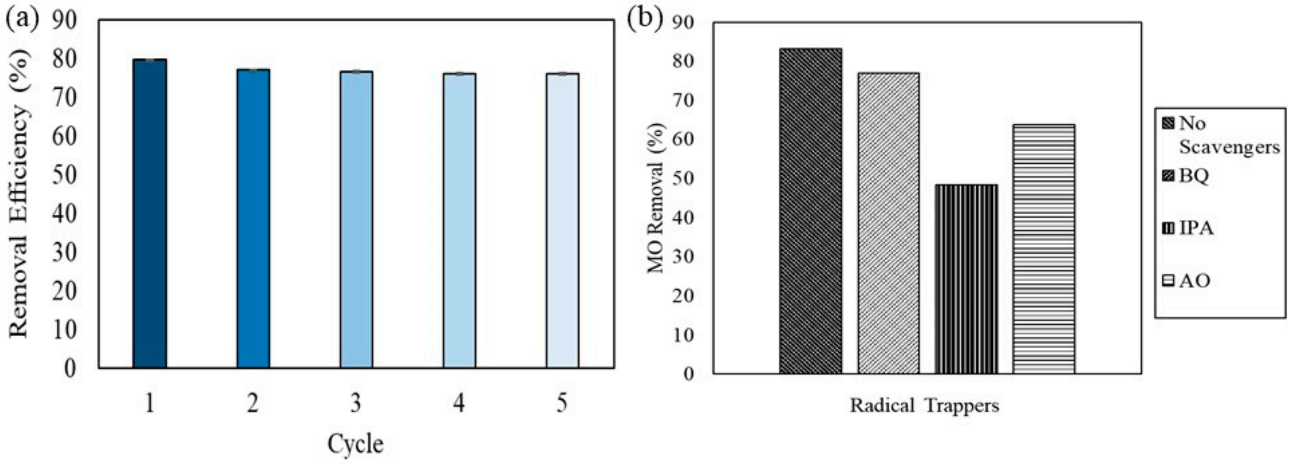

Figure 10. (**a**) Recyclability test of BC-Fe-Zn for five cycles and (**b**) influence of different radical scavengers on the photocatalytic removal of MO (catalyst loading = 1 g/L, pH = 7, scavenger dosage = 0.35 g/L, MO concentration = 10 ppm, reaction time = 120 min, temperature = 25 °C, stirring = 250 rpm).

To determine and understand the generation of different radical scavengers during the photocatalytic removal of MO using the composite photocatalyst, a series of radical trapping agents were added in multiple experiments to determine the radicals generated during the photocatalytic removal of MO with BC-Fe-Zn. Constant amounts of radical scavengers such as isopropyl alcohol (IPA) (•OH), benzoquinone (BQ) ($O_2^{\bullet -}$), and ammonium oxalate (AO) (h^+) were added to the photocatalytic reactor separately. According to the results elucidated in Figure 10a, the removal efficiency of BC-Fe-Zn under the presence of BQ, IPA and AO reduced when compared to experimentation results without any radical trapping agents. In the absence of any radical trappers, a removal efficiency of 83% was observed by BC-Fe-Zn, while the presence of BQ, IPA and AO reduced the removal efficiency to 76%, 48% and 63%, respectively. The results indicate that while the presence of BQ reduced the removal efficiency, the presence of both IPA and AO had a more significant impact on the removal efficiency of MO. This result indicates that •OH and h^+ play the most significant role in removing MO during the reaction, while $O_2^{\bullet -}$ plays a minor role in its removal. Similar observations were reported by Wang et al., who used a FeCu@BC photocatalyst for the remediation of tetracycline [45]. Similar research outcomes on radical quenching experiments were also highlighted by Song et al., which underlined the importance of these radicals to attack dye molecules and degrade them via mineralization [55]. Other research work using BC as a template or substrate also suggest similar photocatalytic removal mechanisms [56,57]. The prepared photocatalyst using a green substrate, namely BC-Fe-Zn, has shown great potential in practical application, as it has exhibited promising performance supplemented with excellent stability and effectiveness in removing MO, which is a common dye found in the textile industry effluent. Hence, BC-Fe-Zn can be considered as a promising photocatalyst for further testing using a more robust textile effluent.

2.5. Benchmarking of Photodegradation of BC–Metal Photocatalyst with Literature

Numerous studies in the literature have investigated the use of BC in the development of photocatalysts. This work compiles and compares the performance and details of various photocatalysts, including those that incorporate BC, and benchmarks them against our findings presented in Table 4. It is worth noting that there is a scarcity of research on bimetallic photocatalysts using BC as a support, especially those featuring Fe. The widespread use of titanium dioxide (TiO_2) nanoparticles in many studies is clearly observed. The data in Table 4 suggest that the performance exhibited in our study is on par with, if not superior to, existing literature. This highlights the remarkable features of BC-Fe-Zn, such as its short degradation time, high efficiency, and outstanding recyclability.

Table 4. Comparative analysis of photocatalytic performances toward organic pollutants: this work vs. literature reports on other BC metal photocatalysts.

Photocatalyst	Biomass Source	Pollutant	Performance (Time)	Recyclability	Reference
BC-Fe-Zn	Wheat straw	MO (10 ppm)	83.33% (120 min)	>90% (5 cycles)	This work
BC-Sn-Fe	Rice husk	Acid Orange 7 (OA7, 10 ppm)	82.22% (120 min)	>70% (5 cycles)	[58]
BC-TiO_2	Microalgae (*Nannochloropsis* sp.)	MB (10 ppm)	90.00% (180 min)	-	[26]
BC-TiO_2	Medium Density Fiberboard (MDF)	MB (10 ppm)	90.00% (180 min)	>80% (3 cycles)	[59]
BC(SB)/g-C_3N_4	Waste biomass	Anthracene (2 ppm)	95.00% (240 min)	>80% (5 cycles)	[60]

3. Methodology

3.1. Materials

BC was obtained from the pyrolysis of wheat straw biomass. Iron (III) nitrate nonahydrate (Fe $(NO_3)_3 \cdot 9H_2O$, ≥98% purity), copper (II) nitrate hexahydrate (Cu $(NO_3)_2 \cdot 6H_2O$, ≥98% purity), chromium (III) nitrate nonahydrate (Cr $(NO_3)_3 \cdot 9H_2O$, ≥98% purity), zinc (II) nitrate hexahydrate (Zn $(NO_3)_2 \cdot 6H_2O$, ≥98% purity), and sodium hydroxide (NaOH, ≥97% purity) were utilized during the synthesis of BC-based photocatalyst. Hydrochloric acid (HCl) and NaOH were used to modify the pH of the MO solution, whereas aluminum oxalate (AO, ≥99% purity) (0.1 mmol), isopropyl alcohol (IPA, ≥99% purity) (0.1 mmol) and ρ-benzoquinone (ρ-BQ, ≥98% purity) were used for radical scavenging experiments. MO, a common dye used in the textile industry, was used as the model pollutant. Ultrapure water from Merck Millipore was used for all experimental processes. All the chemicals used were procured from Sigma-Aldrich (St. Louis, MO, USA) and used without any further modification or purification.

3.2. Synthesis of BC Photocatalyst

3.2.1. Preparation of BC

Wheat straw (WS) pellets (7 mm OD and approximately 12 mm long) were used as raw feedstock for the char production. The WS pellets were manufactured without using any binder. The *as*-received biomass was directly pyrolyzed (500 °C, N_2 atmosphere, 120 min) without any preliminary milling step. This process was implemented to optimize the carbonization efficiency, resulting in a final char with fixed-carbon content of 75.2% determined using a CHNS elemental analyzer [61]. The collected BC was then cooled to room temperature (23 °C), washed with ultrapure water, dried at 80 °C, and ground using an agate mortar before being sieved using a 300 mesh filter.

3.2.2. Synthesis of BC-Fe Photocatalyst with Metallic Dopants

BC photocatalysts were prepared via a modified co-precipitation process which has been described elsewhere [62]. All the BC samples produced in this work use Fe as the primary metal. Using the Fe-Cu bimetal catalyst as an example, 25 mL of 0.4 M Fe $(NO_3)_3 \cdot 9H_2O$ and 25 mL of 0.2 M Cu $(NO_3)_2 \cdot 6H_2O$ solutions (the total metal component in each photocatalyst was 0.6 M) were prepared separately before being magnetically stirred inside a beaker of 100 mL in volume. The molar ratio between Fe and subsequent dopant were kept at 2:1 based on previous literature [63]. This was followed up with the addition of 1.5 g of the BC. The pH of the solution was controlled at 12 via dropwise additions of 6 M of NaOH. The mixture was then heated to 80 °C and maintained at this temperature for 1 h with a constant stirring rate at 250 rpm. The mixture was then cooled to room temperature. The precipitate was washed with ultrapure water to remove residual ions prior to drying at 100 °C for 24 h and being ground into powder using a pestle and mortar. The final samples were calcined at 500 °C for 2 h at a ramping rate of 5 °C/min under a nitrogen atmosphere. A mass ratio of 1:3 was maintained for the metal dopants to BC throughout the preparation of catalysts in this study. The mass of the Fe salt used was kept constant through the work. The ratio of metal dopants was controlled based on the molar mass of metals in its salts. The synthesis process was repeated by replacing Cu $(NO_3)_2 \cdot 6H_2O$ with Cr $(NO_3)_3 \cdot 9H_2O$ and Zn $(NO_3)_2 \cdot 6H_2O$ for the preparation of photocatalysts with other metallic dopants. The samples are denoted in Table 5. Figure 11 shows the process of preparing the BC catalysts in this study.

Table 5. Denotations of photocatalyst prepared in this work, including pristine BC.

Sample Name	Metal Dopant	Sample Denomination
Biochar	Nil	BC
Biochar-Fe	Fe	BC-Fe
Biochar-Fe-Cu	Fe, Cu	BC-Fe-Cu
Biochar-Fe-Cr	Fe, Cr	BC-Fe-Cr
Biochar-Fe-Zn	Fe, Zn	BC-Fe-Zn

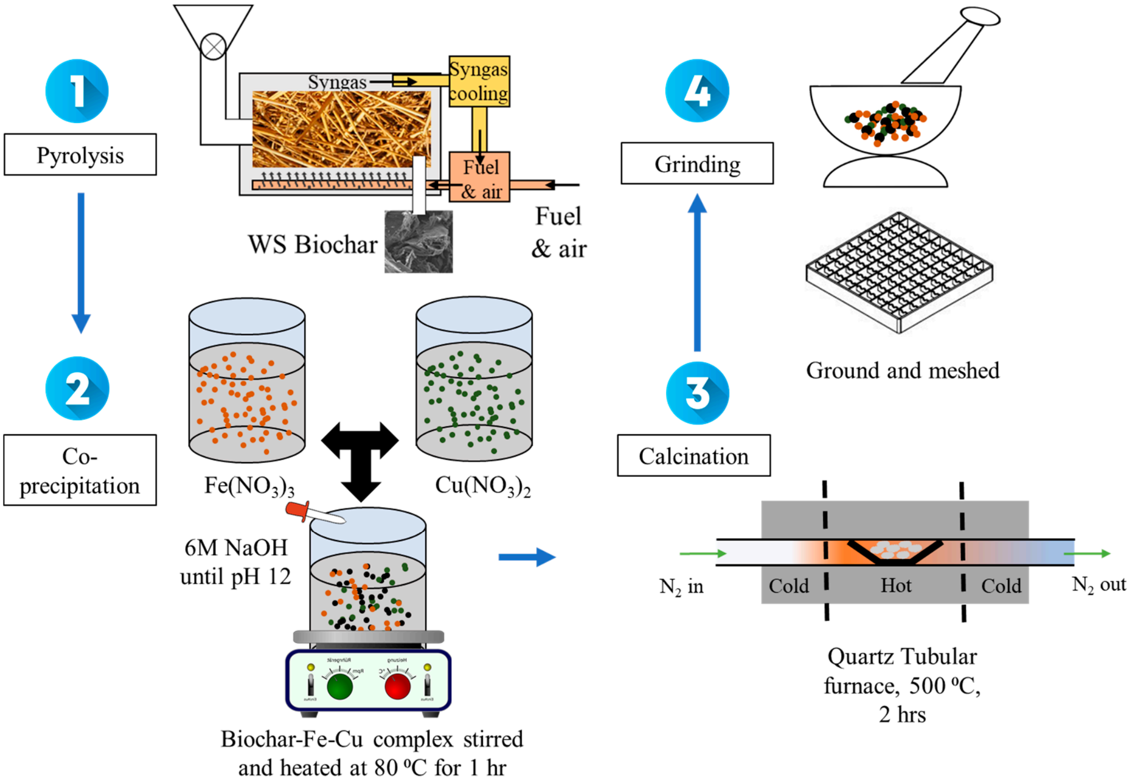

Figure 11. Synthesis of the BC catalysts in this work: (1) pyrolysis of wheat straw husk, (2) co-precipitation of preparing BC-metal catalysts, (3) sintering of prepared photocatalyst at 500 °C, (4) grinding and meshing of prepared photocatalyst.

3.3. Characterization of Synthesized Catalyst

The microstructures of the BC-based photocatalyst were examined using a Jeol JSM7600f Scanning Electron Microscope (SEM). High-resolution images of the catalyst were captured using a HT 7700 Transmission Electron Microscope (TEM) from Hitachi. An aluminum stub with a carbon tape was used to hold the samples. The dispersion of dopants was examined by energy-dispersive X-ray (Oxford Instruments 400) analysis. The phase and crystallinity of samples prepared were determined using X-ray powder diffraction (Bruker D8 Advance). The diffraction patterns were recorded in the 2θ range of 10° to 80° with a speed of 5 ° per min, a step size of 0.05 ° and a glancing angle of 5°. Furthermore, the crystalline size of the composite photocatalyst was determined using Scherrer's equation, which is given in Equation (1);

$$Dhkl = \frac{K\lambda}{Bhkl cos\theta}\% \tag{1}$$

where $Dhkl$ is the crystallite size in the direction perpendicular to the lattice planes, hkl are the Miller indices of the planes being analyzed, K is a numerical factor frequently referred to as the crystallite-shape factor, λ is the wavelength of the X-rays, $Bhkl$ is the width (full-width at half-maximum) of the X-ray diffraction peak in radians, and θ is the Bragg angle. The SSA and particle pore characteristics were examined via the Brunauer–Emmett–Teller method (Quantachrome Nova 4000e Porosimeter). The maximum temperature of 120 °C at a heating rate of 5 °C/min was employed for degassing purposes. The average pore volume and size of doped BC was determined using Barret–Joyner–Halender (BJH) method. The optical properties of the prepared photocatalyst were evaluated using (UV–Vis NIR, Perkin Elmer Lambda 1050) to determine the absorption wavelength and fluorescence spectroscopy (HORIBA Steady State Fluorescence spectrometers) to determine the response of photocatalyst in visible light range.

3.4. Photocatalytic Tests

3.4.1. Preparation of the Model Pollutant

The changes in MO concentrations were determined using an ultraviolet-visible spectrophotometer (Thermo Fisher Evolution 220 UV-Vis Spectrophotometer, Waltham, MA, USA). MO solutions of different concentrations (0, 2, 4, 6, 8, 10 ppm) were prepared using ultrapure water and were used for calibration. MO samples of 10, 20, 30, 40 and 50 ppm were also prepared to investigate the influence of pollutant concentrations on the photocatalytic performance of the catalysts.

3.4.2. Adsorption Studies

An adsorption test was carried out to determine the maximum amount of MO adsorbed by the photocatalyst before the initiation of photocatalytic reaction. First, 0.2 g of the BC was dispersed into 200 mL (1.0 g/L) of 10 ppm MO and stirred on a magnetic stirrer at 250 rpm. The adsorption experiment was conducted under a dark condition to avoid activation of the photocatalyst. Aliquots of 10 mL were collected at an interval of 5 min using a 15 mL syringe fitted with a polytetrafluoroethylene (PTFE) filter (pore size of 0.45 µm) to remove photocatalyst particles. The adsorption test was performed for all the prepared photocatalysts in this study. The MO removal via adsorption was calculated based on Equation (2).

$$M_r = \frac{M_o - M_i}{M_o} \times 100\ \% \tag{2}$$

where M_r is the reduction of MO, M_o is the initial absorbance reading displayed by the UV–vis spectrophotometer, and M_i is the absorbance reading of the sample. The data collected from adsorption experiments were fitted into the first and second-order models to determine the adsorption mechanism. Lagergren pseudo-first order (Equation (3)) and pseudo-second order kinetic (Equation (4)) models were used for the kinetic studies

$$\ln\,(q_e - q_t) = \ln q_e - k_1 t \tag{3}$$

$$\frac{t}{q_t} = \frac{1}{k_2 q^2 e} + \frac{t}{q_e} \tag{4}$$

where q_e and q_t represent the amount of MO adsorbed (mg/g) at equilibrium and at a given time, t(h), respectively, whereas k_1 is the rate constant of pseudo-first-order model (1/h) and k_2 is the rate constant for pseudo-second-order model (g/mg·h) [64].

3.4.3. Evaluation of Photocatalytic Activity

The photocatalytic activity of BC and the prepared photocatalysts with different metal dopants was evaluated based on the photocatalytic removal of MO under visible light irradiation. A 300 W LED lamp was used as the source of visible light. The reaction was carried out inside a black chamber which houses the reactor and light source. In a typical experiment, 0.2 g of material (1.0 g/L) was added into 200 mL of 10 ppm MO. 2 mL of 1 M hydrogen peroxide (H_2O_2) was added to initiate photoactivity. The light was turned on once the predetermined adsorption time has passed (based on results from Section 3.4.2) to initiate photocatalytic activity. The changes in MO concentration before and after photocatalytic experiments were determined using an ultraviolet-visible spectrophotometer. The photocatalytic experiments were also repeated with different initial pH values (3,7,11) and different initial concentrations of MO (10,20, 30, 40, 50 ppm). The kinetics and photocatalytic decolorization rate of MO were determined using the Langmuir–Hinshelwood kinetics model, as given in Equation (5).

$$\ln\left(\frac{C_o}{C_t}\right) = k_{app} t \tag{5}$$

where C_o is the initial concentration of MO, and C_t is the concentration at known time t while k_{app} is the apparent rate constant. The pseudo-first-order rate constant k_{app} (min^{-1}) was calculated based on the slope of ln (C_o/C_t) versus irradiation time, t.

3.4.4. Reactive Oxidative Species Determination

The main radical species responsible toward the photocatalytic removal of MO was investigated by employing radical scavengers during photocatalytic removal. To study the roles of h^+, OH^-, and $\bullet O^{2-}$ radical species, scavengers such as AO (0.1 mmol), IPA (0.1 mmol) and ρ-BQ (0.1 mmol) were individually added into the photocatalytic reaction system. The experiments were carried out according to the method described in Section 3.4.3.

3.4.5. Photocatalyst Recyclability Analysis

The recyclability of the heterogeneous photocatalyst prepared was evaluated by repeating the experiments five times using the same spent catalyst. In a typical experiment, 0.2 g of material (1.0 g/L) was added into 200 mL of 10 ppm MO. Then, 2 mL of 1 M hydrogen peroxide (H_2O_2) was added followed by turning on the light source to initiate photoactivity. When the experiment time lapsed (120 min), 10 mL of MO sample was collected from the beaker to be analyzed, while the remainder of the solution was filtered using filter paper, triple rinsed with ultrapure water and then dried in an oven at 100 °C for 24 h. The dried samples were then ground using a pestle and mortar and reused for the subsequent experiments.

4. Conclusions

BC as a green substrate and carbon-based dopant has been employed for hosting an Fe photocatalyst through a single-step co-precipitation method with Cu, Cr, and Zn also used as secondary dopants to enhance its photocatalytic activity under visible light. MO served as the model pollutant to assess the photocatalytic performance of the catalysts prepared. Scanning electron microscopy images illustrated the formation of a uniform metal catalyst on the BC surface, while the energy-dispersive X-ray spectroscopy mapping demonstrated the even dispersion of the catalyst. X-ray diffraction analysis indicated a robust interaction between BC, Fe, and the dopants (Cu, Cr, Zn), revealing characteristic peaks of all metals present in the photocatalyst. BET analysis showcased a substantial increase in the catalyst's surface area post-co-precipitation, which was attributed to the use of a strong alkali reagent during the process. This reagent facilitated impurity removal, exposing pores and channels (from 41.07 to 117.99 m^2/g). Kubelka–Munk plots disclosed band gap values of 2.423, 2.421, 2.424, and 2.403 eV for BC-Fe, BC-Fe-Cu, BC-Fe-Cr, and BC-Fe-Zn, respectively. Photoluminescence spectra revealed absorption peaks and emissions in the visible light region, indicating the prepared photocatalyst's responsiveness to visible light irradiation. Photocatalytic experiments demonstrated that BC-Fe-Zn exhibited the highest removal rate and efficiency, achieving an 83.3% removal of MO within 120 min of irradiation. Parametric studies suggested that a pH of 12 optimally facilitated photocatalytic activity, and at a loading of 1.0 g/L, the catalyst remained effective in removing MO up to 30 ppm in aqueous conditions. These results conclude that the development of a stable and viable BC-based photocatalyst using wheat straw exhibits clear potential to be used for wastewater remediation via photocatalysis.

Author Contributions: M.N.S. Subramaniam and Z.W. were responsible for original draft preparation, investigation and validation. J.Z. was responsible for data curation and validation. Z.W., P.S.G. and G.Z. were responsible for review, editing and funding acquisition. All authors have read and agreed to the published version of the manuscript.

Funding: The authors would like to acknowledge the support by the European Union (Open Innovation Test Bed for nano-enabled Membranes-862330) and State Key Laboratory of Material-Oriented Chemical Engineering (KL18-10).

Data Availability Statement: The authors can confirm that all relevant data are included in the article.

Conflicts of Interest: The authors do not have any financial or non-financial interests that are directly or indirectly related to the work submitted for publication.

References

1. van Vliet, M.T.H.; Jones, E.R.; Flörke, M.; Franssen, W.H.P.; Hanasaki, N.; Wada, Y.; Yearsley, J.R. Global Water Scarcity Including Surface Water Quality and Expansions of Clean Water Technologies. *Environ. Res. Lett.* **2021**, *16*, 024020. [CrossRef]
2. Ambigadevi, J.; Senthil Kumar, P.; Vo, D.-V.N.; Hari Haran, S.; Srinivasa Raghavan, T.N. Recent Developments in Photocatalytic Remediation of Textile Effluent Using Semiconductor Based Nanostructured Catalyst: A Review. *J. Environ. Chem. Eng.* **2021**, *9*, 104881. [CrossRef]
3. Ighnih, H.; Haounati, R.; Malekshah, R.E.; Ouachtak, H.; Jada, A.; Addi, A.A. Photocatalytic Degradation of RhB Dye Using Hybrid Nanocomposite BiOCl@Kaol under Sunlight Irradiation. *J. Water Process Eng.* **2023**, *54*, 103925. [CrossRef]
4. Al-Tohamy, R.; Ali, S.S.; Li, F.; Okasha, K.M.; Mahmoud, Y.A.G.; Elsamahy, T.; Jiao, H.; Fu, Y.; Sun, J. A Critical Review on the Treatment of Dye-Containing Wastewater: Ecotoxicological and Health Concerns of Textile Dyes and Possible Remediation Approaches for Environmental Safety. *Ecotoxicol. Environ. Saf.* **2022**, *231*, 113160. [CrossRef] [PubMed]
5. Peng, Y.; Sun, Y.; Hanif, A.; Shang, J.; Shen, Z.; Hou, D.; Zhou, Y.; Chen, Q.; Ok, Y.S.; Tsang, D.C.W. Design and Fabrication of Exfoliated Mg/Al Layered Double Hydroxides on Biochar Support. *J. Clean. Prod.* **2021**, *289*, 125142. [CrossRef]
6. Ou, S.-F.; Yang, D.-S.; Liao, J.-W.; Chen, S.-T. Treating High COD Dyeing Wastewater via a Regenerative Sorption-Oxidation Process Using a Nano-Pored Activated Carbon. *Int. J. Mol. Sci.* **2022**, *23*, 4752. [CrossRef]
7. Karam, A.; Bakhoum, E.S.; Zaher, K. Coagulation/Flocculation Process for Textile Mill Effluent Treatment: Experimental and Numerical Perspectives. *Int. J. Sustain. Eng.* **2021**, *14*, 983–995. [CrossRef]
8. Katiyar, J.; Saharan, V.K. Enhanced Photocatalytic Degradation of Reactive Blue 21 Dye and Textile Dyeing Effluent by Synthesized SmFeO3-RGO Photocatalyst in Combination with Ultrasonication: Characterization and Performance Evaluation. *J. Water Process Eng.* **2023**, *56*, 104314. [CrossRef]
9. Acharya, S.M.; Chakraborty, R.; Tringe, S.G. Emerging Trends in Biological Treatment of Wastewater From Unconventional Oil and Gas Extraction. *Front. Microbiol.* **2020**, *11*, 569019. [CrossRef]
10. Pipil, H.; Yadav, S.; Chawla, H.; Taneja, S.; Verma, M.; Singla, N.; Haritash, A.K. Comparison of TiO_2 Catalysis and Fenton's Treatment for Rapid Degradation of Remazol Red Dye in Textile Industry Effluent. *Rend. Lincei. Sci. Fis. Nat.* **2022**, *33*, 105–114. [CrossRef]
11. Khlyustova, A.; Sirotkin, N.; Kusova, T.; Kraev, A.; Titov, V.; Agafonov, A. Doped TiO_2: The Effect of Doping Elements on Photocatalytic Activity. *Mater. Adv.* **2020**, *1*, 1193–1201. [CrossRef]

12. Wang, Y.; Liang, L.; Dai, H.; Li, N.; Song, Y.; Yan, B.; Chen, G.; Hou, L. Activation of Peroxymonosulfate by Food Waste Digestate Derived Biochar for Sulfamethoxazole Degradation: Performance and Mechanism. *Sep. Purif. Technol.* **2023**, *327*, 124935. [CrossRef]
13. Yaashikaa, P.R.; Kumar, P.S.; Varjani, S.; Saravanan, A. A Critical Review on the Biochar Production Techniques, Characterization, Stability and Applications for Circular Bioeconomy. *Biotechnol. Rep.* **2020**, *28*, e00570. [CrossRef] [PubMed]
14. Janu, R.; Mrlik, V.; Ribitsch, D.; Hofman, J.; Sedláček, P.; Bielská, L.; Soja, G. Biochar Surface Functional Groups as Affected by Biomass Feedstock, Biochar Composition and Pyrolysis Temperature. *Carbon Resour. Convers.* **2021**, *4*, 36–46. [CrossRef]
15. Bharathi, D.; Lee, J.; Karthiga, P.; Sandhanasamy, R.M. Kiwi Fruit Peel Biowaste Mediated Green Synthesis of Silver Nanoparticles for Enhanced Dye Degradation and Antibacterial Activity. *Waste Biomass Valoriz.* **2023**, *2023*, 1–10. [CrossRef]
16. Ghumro, S.S.; Lal, B.; Pirzada, T. Visible-Light-Driven Carbon-Doped TiO_2-Based Nanocatalysts for Enhanced Activity toward Microbes and Removal of Dye. *ACS Omega* **2022**, *7*, 4333–4341. [CrossRef] [PubMed]
17. Salunkhe, T.T.; Gurugubelli, T.R.; Babu, B.; Yoo, K. Recent Innovative Progress of Metal Oxide Quantum-Dot-Integrated g-C3N4 (0D-2D) Synergistic Nanocomposites for Photocatalytic Applications. *Catalysts* **2023**, *13*, 1414. [CrossRef]
18. Albero, J.; Mateo, D.; García, H. Graphene-Based Materials as Efficient Photocatalysts for Water Splitting. *Molecules* **2019**, *24*, 906. [CrossRef]
19. Lu, K.; Li, Y.; Tang, Z.; Xu, Y. Roles of Graphene Oxide in Heterogeneous Photocatalysis. *ACS Mater.* **2021**, *1*, 37–54. [CrossRef]
20. Saini, D.; Garg, A.K.; Dalal, C.; Anand, S.R.; Sonkar, S.K.; Sonker, A.K.; Westman, G. Visible-Light-Promoted Photocatalytic Applications of Carbon Dots: A Review. *ACS Appl. Nano Mater.* **2022**, *5*, 3087–3109. [CrossRef]
21. Yao, Y.; Zhang, H.; Hu, K.; Nie, G.; Yang, Y.; Wang, Y.; Duan, X.; Wang, S. Carbon Dots Based Photocatalysis for Environmental Applications. *J. Environ. Chem. Eng.* **2022**, *10*, 107336. [CrossRef]
22. Phin, H.-Y.; Ong, Y.-T.; Sin, J.-C. Effect of Carbon Nanotubes Loading on the Photocatalytic Activity of Zinc Oxide/Carbon Nanotubes Photocatalyst Synthesized via a Modified Sol-Gel Method. *J. Environ. Chem. Eng.* **2020**, *8*, 103222. [CrossRef]
23. Zhao, F.; Yang, Y.; Ji, S.; Yu, R.; Li, X.; Zhou, Z. Photocatalysis-Fenton Mechanism of RGO-Enhanced Fe-Doped Carbon Nitride with Boosted Degradation Performance towards Rhodamine B. *J. Water Process Eng.* **2023**, *55*, 104080. [CrossRef]
24. Mondal, A.; Prabhakaran, A.; Gupta, S.; Subramanian, V.R. Boosting Photocatalytic Activity Using Reduced Graphene Oxide (RGO)/Semiconductor Nanocomposites: Issues and Future Scope. *ACS Omega* **2021**, *6*, 8734–8743. [CrossRef] [PubMed]
25. Yu, L.; Xu, W.; Liu, H.; Bao, Y. Titanium Dioxide–Reduced Graphene Oxide Composites for Photocatalytic Degradation of Dyes in Water. *Catalysts* **2022**, *12*, 1340. [CrossRef]
26. Pinna, M.; Binda, G.; Altomare, M.; Marelli, M.; Dossi, C.; Monticelli, D.; Spanu, D.; Recchia, S. Biochar Nanoparticles over TiO_2 Nanotube Arrays: A Green Co-Catalyst to Boost the Photocatalytic Degradation of Organic Pollutants. *Catalysts* **2021**, *11*, 1048. [CrossRef]
27. Wang, W.; Zhang, J.; Chen, T.; Sun, J.; Ma, X.; Wang, Y.; Wang, J.; Zhonglei, X. Preparation of TiO_2 -Modified Biochar and Its Characteristics of Photo-Catalysis Degradation for Enrofloxacin. *Sci. Rep.* **2020**, *10*, 6588. [CrossRef] [PubMed]
28. Jamdagni, P.; Rana, J.S.; Khatri, P. Comparative Study of Antifungal Effect of Green and Chemically Synthesised Silver Nanoparticles in Combination with Carbendazim, Mancozeb, and Thiram. *IET Nanobiotechnol.* **2018**, *12*, 1102–1107. [CrossRef]
29. Fatimah, I.; Purwiandono, G.; Sahroni, I.; Wijayana, A.; Faraswati, M.; Dwi Putri, A.; Oh, W.-C.; Doong, R. Magnetically-Separable Photocatalyst of Magnetic Biochar from Snake Fruit Peel for Rhodamine B Photooxidation. *Environ. Nanotechnol. Monit. Manag.* **2022**, *17*, 100669. [CrossRef]
30. Adepu, A.K.; Goskula, S.; Chirra, S.; Siliveri, S.; Gujjula, S.R.; Narayanan, V. Synthesis of a High-Surface Area V_2O_5/TiO_2-SiO_2 Catalyst and Its Application in the Visible Light Photocatalytic Degradation of Methylene Blue. *RSC Adv.* **2019**, *9*, 24368–24376. [CrossRef]
31. Zhao, X.; Han, R. Characterization of Bio-Char from Pyrolysis of Wheat Straw and Its Evaluation on Methylene Blue Adsorption. *Desalinat. Water Treat.* **2012**, *46*, 115–123. [CrossRef]
32. Armynah, B.; Djafar, Z.; Piarah, W.H. Analysis of Chemical and Physical Properties of Biochar from Rice Husk Biomass Analysis of Chemical and Physical Properties of Biochar from Rice Husk Biomass. *J. Phys. Conf. Ser. Pap.* **2018**, *979*, 012038. [CrossRef]
33. Phul, R.; Kaur, C.; Farooq, U.; Ahmad, T. Ascorbic Acid Assisted Synthesis, Characterization and Catalytic Application of Copper Nanoparticles. *Mater. Sci. Eng. Int. J.* **2018**, *2*, 90–94.
34. Nomura, K. Self-Dual Leonard Pairs Green Synthesis of Copper Oxide Nanoparticles Extract Assessment and Biological Properties. *De Gruyter* **2019**, *8*, 557–567.
35. Bansal, J.; Tabassum, R.; Swami, S.K.; Bishnoi, S.; Vashishtha, P.; Gupta, G.; Sharma, S.N.; Hafiz, A.K. Performance Analysis of Anomalous Photocatalytic Activity of Cr-Doped TiO_2 Nanoparticles [$Cr_{(x)}TiO_{2(1-x)}$]. *Appl. Phys. A Mater. Sci. Process.* **2020**, *126*, 363. [CrossRef]
36. Muhammad, W.; Ullah, N.; Haroon, M.; Abbasi, B.H. Optical, Morphological and Biological Analysis of Zinc Oxide Nanoparticles (ZnO NPs) Using Papaver. *RSC Adv.* **2019**, *9*, 29541–29548. [CrossRef] [PubMed]
37. Tomczyk, A. Biochar Physicochemical Properties: Pyrolysis Temperature and Feedstock Kind Effects. *Rev. Environ. Sci. Biol. Technol.* **2020**, *19*, 191–215. [CrossRef]
38. Liu, C.; Wang, W.; Wu, R.; Liu, Y.; Lin, X.; Kan, H.; Zheng, Y. Preparation of Acid- and Alkali-Modified Biochar for Removal of Methylene Blue Pigment. *ACS Omega* **2020**, *5*, 30906–30922. [CrossRef]

39. Wei, X.; Yu, F.; Ji, J.; Cai, Y.; Zou, W.; Zheng, Y.; Huang, J.; Zhang, Y.; Yang, Y.; Naushad, M.; et al. Porous Biochar Supported Ag3PO4 Photocatalyst for "Two-in-One" Synergistic Adsorptive-Photocatalytic Removal of Methylene Blue under Visible Light Irradiation. *J. Environ. Chem. Eng.* **2021**, *9*, 106753. [CrossRef]
40. Zehtab-Lotfi, E.; Amani-Ghadim, A.R.; Soltani, B. Visible Light-Driven Photocatalytic Activity of Wide Band Gap $ATiO_3$ (A = Sr, Zn and Cd) Perovskites by Lanthanide Doping and the Formation of a Mesoporous Heterostructure with ZnS QDs. *Dalt. Trans.* **2022**, *51*, 12198–12212. [CrossRef]
41. Lai, M.T.L.; Lee, K.M.; Yang, T.C.K.; Pan, G.T.; Lai, C.W.; Chen, C.-Y.; Johan, M.R.; Juan, J.C. The Improved Photocatalytic Activity of Highly Expanded $MoS_{(2)}$ under Visible Light Emitting Diodes. *Nanoscale Adv.* **2021**, *3*, 1106–1120. [CrossRef]
42. Lu, Y.; Cai, Y.; Zhang, S.; Zhuang, L.; Hu, B.; Wang, S.; Chen, J.; Wang, X. Application of Biochar-Based Photocatalysts for Adsorption-(Photo)Degradation/Reduction of Environmental Contaminants: Mechanism, Challenges and Perspective. *Biochar* **2022**, *4*, 45. [CrossRef]
43. Talukdar, K.; Jun, B.-M.; Yoon, Y.; Kim, Y.; Fayyaz, A.; Park, C.M. Novel Z-Scheme Ag_3PO_4/Fe_3O_4-Activated Biochar Photocatalyst with Enhanced Visible-Light Catalytic Performance toward Degradation of Bisphenol A. *J. Hazard. Mater.* **2020**, *398*, 123025. [CrossRef] [PubMed]
44. Nguyen, V.H.; Nguyen, T.D.; Bach, L.G.; Hoang, T.; Bui, Q.T.P.; Tran, L.D.; Nguyen, C.V.; Vo, D.V.N.; Do, S.T. Effective Photocatalytic Activity of Mixed Ni/Fe-Base Metal-Organic Framework under a Compact Fluorescent Daylight Lamp. *Catalysts* **2018**, *8*, 487. [CrossRef]
45. Wang, Y.; Qiao, L.; Zhang, X.; Liu, Z.; Li, T.; Wang, H. Green Synthesis of FeCu@biochar Nanocomposites through a Mechanochemical Method for Enhanced Tetracycline Degradation via Peroxymonosulfate Activation. *Sep. Purif. Technol.* **2024**, *328*, 125077. [CrossRef]
46. Monteiro, F.C.; Guimaraes, I.D.L.; de Almeida Rodrigues, P.; da Anunciação de Pinho, J.V.; Conte-Junior, C.A. Degradation of PAHs Using TiO_2 as a Semiconductor in the Heterogeneous Photocatalysis Process: A Systematic Review. *J. Photochem. Photobiol. A Chem.* **2023**, *437*, 114497. [CrossRef]
47. Modrogan, C.; Căprărescu, S.; Purcar, V.; Radit, V. Modified Composite Based on Magnetite and Polyvinyl Alcohol: Synthesis, Characterization, and Degradation Studies of the Methyl Orange Dye from Synthetic Wastewater. *Polymers* **2021**, *13*, 3911. [CrossRef]
48. Li, M.; Dong, B.; Chang, Z.; Dang, H.; Ma, S.; Li, W. Synthesis of $TiO_2/g\text{-}C_3N_4$ Photocatalyst with Recovered TiO2 from Spent SCR Catalyst for Photodegrading Rhodamine B. *Waste Biomass Valoriz.* **2023**, *14*, 687–701. [CrossRef]
49. Wang, X.; Yang, Z.; Jiang, Y.; Zhao, P.; Meng, X. Adsorption and Catalytic Degradation of Phenol in Water by a Mn, N Co-Doped Biochar via a Non-Radical Oxidation Process. *Sep. Purif. Technol.* **2024**, *330*, 125267. [CrossRef]
50. Saeed, M.; Muneer, M.; Mumtaz, N.; Siddique, M.; Akram, N.; Hamayun, M. Ag-Co_3O_4: Synthesis, Characterization and Evaluation of Its Photo-Catalytic Activity towards Degradation of Rhodamine B Dye in Aqueous Medium. *Chinese J. Chem. Eng.* **2018**, *26*, 1264–1269. [CrossRef]
51. Zhang, C.; Ma, Y.; Li, C.; Qin, F.; Hu, C.; Hu, Q.; Duo, S. Spatially Confined Growth of Bi_2O_4 into Hierarchical TiO_2 Spheres for Improved Visible Light Photocatalytic Activity. *J. Mater. Sci.* **2020**, *55*, 3181–3194. [CrossRef]
52. Vorontsov, A.V.; Valdés, H.; Smirniotis, P.G.; Paz, Y. Recent Advancements in the Understanding of the Surface Chemistry in TiO2 Photocatalysis. *Surfaces* **2020**, *3*, 72–92. [CrossRef]
53. Youssef, N.A.; Shaban, S.A.; Ibrahim, F.A.; Mahmoud, A.S. Degradation of Methyl Orange Using Fenton Catalytic Reaction. *Egypt. J. Pet.* **2016**, *25*, 317–321. [CrossRef]
54. Cui, X.; Wang, Y.; Jiang, G.; Zhao, Z.; Xu, C.; Duan, A.; Liu, J.; Wei, Y.; Bai, W. The Encapsulation of CdS in Carbon Nanotubes for Stable and Efficient Photocatalysis. *J. Mater. Chem. A* **2014**, *2*, 20939–20946. [CrossRef]
55. Song, C.; Chen, K.; Chen, M.; Jin, X.; Liu, G.; Du, X.; Chen, D.; Huang, Q. Sequential Combined Adsorption and Solid-Phase Photocatalysis to Remove Aqueous Organic Pollutants by H3PO4-Modified TiO_2 Nanoparticles Anchored on Biochar. *J. Water Process Eng.* **2022**, *45*, 102467. [CrossRef]
56. Asgharzadeh, F.; Rezaei, R.; Gholami, M.; Jafari, A.J.; Kermani, M. TiO_2—Decorated Magnetic Biochar Mediated Heterogeneous Photocatalytic Degradation of Tetracycline and Evaluation of Antibacterial Activity. *Biomass Convers. Biorefinery* **2021**, *2021*, 1–11. [CrossRef]
57. Asgharzadeh, F.; Gholami, M.; Jonidi, A.; Kermani, M. Heterogeneous Photocatalytic Degradation of Metronidazole from Aqueous Solutions Using Fe_3O_4/TiO_2 Supported on Biochar. *Desalinat. Water Treat.* **2020**, *175*, 24789. [CrossRef]
58. Sadati, H.; Ayati, B. Using a Promising Biomass-Based Biochar in Photocatalytic Degradation: Highly Impressive Performance of RHB/SnO_2/Fe_3O_4 for Elimination of AO7. *Photochem. Photobiol. Sci.* **2023**, *22*, 1445–1462. [CrossRef]
59. Silvestri, S.; Stefanello, N.; Sulkovski, A.A.; Foletto, E.L. Preparation of TiO_2 Supported on MDF Biochar for Simultaneous Removal of Methylene Blue by Adsorption and Photocatalysis. *J. Chem. Technol. Biotechnol.* **2020**, *95*, 2723–2729. [CrossRef]
60. Syed Abd Halim, S.N.Q.; Nazri, N.A.M.; Nordin, N.A.H.M. Photocatalytic Degradation of Anthracene by Biochar-Based Graphitic Carbon Nitride. *IOP Conf. Ser. Mater. Sci. Eng.* **2021**, *1195*, 012053. [CrossRef]
61. Rego, F.; Xiang, H.; Yang, Y.; Ordovás, J.L.; Chong, K.; Wang, J.; Bridgwater, A. Investigation of the Role of Feedstock Properties and Process Conditions on the Slow Pyrolysis of Biomass in a Continuous Auger Reactor. *J. Anal. Appl. Pyrolysis* **2022**, *161*, 105378. [CrossRef]

62. Leichtweis, J.; Silvestri, S.; Welter, N.; Vieira, Y.; Zaragoza-sánchez, P.I.; Chávez-mejía, A.C.; Carissimi, E. Wastewater Containing Emerging Contaminants Treated by Residues from the Brewing Industry Based on Biochar as a New $CuFe_2O_4$/Biochar Photocatalyst. *Process Saf. Environ. Prot.* **2021**, *150*, 497–509. [CrossRef]
63. Nguyen, M.B.; Le, G.H.; Nguyen, T.D.; Nguyen, Q.K.; Pham, T.T.T.; Lee, T.; Vu, T.A. Bimetallic Ag-Zn-BTC/GO Composite as Highly Efficient Photocatalyst in the Photocatalytic Degradation of Reactive Yellow 145 Dye in Water. *J. Hazard. Mater.* **2021**, *420*, 126560. [CrossRef]
64. Revellame, E.D.; Fortela, D.L.; Sharp, W.; Hernandez, R.; Zappi, M.E. Adsorption Kinetic Modeling Using Pseudo-First Order and Pseudo-Second Order Rate Laws: A Review. *Clean. Eng. Technol.* **2020**, *1*, 100032. [CrossRef]